

# Tunneling and dark currents in HgCdTe photodiodes

Y. Nemirovsky, D. Rosenfeld, R. Adar, and A. Kornfeld

*Kidron Microelectronics Research Center, Department of Electrical Engineering, Technion-Israel Institute of Technology, Haifa 32000, Israel*

(Received 11 October 1988; accepted 14 November 1988)

The dc characteristics of front-illuminated ion-implanted  $n^+$  on bulk  $p$ -type  $\text{Hg}_{1-x}\text{Cd}_x\text{Te}$  with  $x \approx 0.22$ , operating at 77 K, are modeled with three distinct mechanisms that dominate the dark current: In the zero- and low-bias region, diffusion current is the dominant current down to 60 K. For medium reverse bias, at 77 K, trap-assisted tunneling produces the dark current and dominates the dark current at zero bias below 50 K. For a high reverse bias, bulk band-to-band tunneling dominates. By measuring the temperature dependence of the dc characteristics in the temperature range 65–132 K, the mechanisms are studied and the validity of the modeling is confirmed. The  $1/f$  noise phenomena measured at high reverse bias are correlated with the bulk band-to-band tunneling current. The electrical profile of the implanted junction is correlated with the origin of the  $p$ -type conductivity and with the dc characteristics.

## I. INTRODUCTION

In current HgCdTe material and device technology, the performance of HgCdTe photodiodes is limited by excess dark currents and the associated noise currents.<sup>1–3</sup>  $\text{Hg}_{1-x}\text{Cd}_x\text{Te}$  ( $x \approx 0.22$ ) photodiodes with cutoff wavelengths in the range 8–12  $\mu\text{m}$ , operating near 77 K, exhibit dc characteristics and noise behavior that are very sensitive to material properties as well as to device processing technology. The origin and mechanism of the above currents are not yet well established. There is a considerable need for a model to correlate the dark and noise currents with the material properties such as composition, band gap, cutoff wavelength, doping concentration, nature of the dopant, excess carrier lifetime, surface potential, etc.

To emphasize the importance of HgCdTe process and device modeling, we should note that the emerging HgCdTe photodiode technology is not yet mature enough to satisfy the wide requirements of advanced infrared focal plane arrays.<sup>4</sup> It is difficult to obtain reproducible, high-quality uniform  $p$ -type substrates with well-controlled material properties, and to process arrays with uniform, high-performance photodiodes, tailored according to system requirements. These requirements are defined in terms of dark currents, dynamic resistance, excess low-frequency noise, quantum efficiency, and cutoff wavelength. The above parameters are interrelated and depend strongly on material properties as well as device processing technology.

The complete technology of diode fabrication such as junction formation, surface passivation, and contacting and metallization is not yet fully established. A given process that yields high-performance diodes in a given starting material must sometimes be modified if the origin of the  $p$ -type material is changed. It is obvious that the processing techniques and the material properties are strongly interrelated. Simple yet quantitative techniques and models are required to characterize the starting material and the individual processing steps, and to correlate the various measured parameters with final device performance, in particular, the dc characteristics and the associated noise performance.

In this paper we model the dark currents of front-illuminated ion-implanted  $n^+$  on bulk  $p$ -type  $\text{Hg}_{1-x}\text{Cd}_x\text{Te}$  with  $x \approx 0.22$  at 77 K. The major fabrication features are described in Sec. II, and the role of the surface passivation is described in Sec. III. Measured junction capacitance–reverse voltage characteristics of an implanted junction, and the resulting junction electrical profile for doped and undoped material are given in Sec. IV.

In Sec. V we consider the mechanisms that produce dark currents in  $\text{Hg}_{1-x}\text{Cd}_x\text{Te}$  photodiodes with  $x \approx 0.22$ , in various bias regions. These mechanisms also determine the dynamic resistance as a function of reverse bias. We model the dc behavior of the diodes and compare the measured and calculated characteristics.

Three distinct mechanisms dominate the dark current. In the zero-bias and low-bias region, diffusion current is the dominant current down to 60 K. For medium reverse bias, trap-assisted tunneling produces the dark current, and also dominates the dark current at zero bias below 50 K. For a high reverse bias, bulk band-to-band tunneling dominates. By measuring the temperature dependence of the dc characteristics in the temperature range 65–132 K, the mechanisms are studied and the validity of the model is confirmed.

In Sec. VI we correlate the mechanism that produces the dc dark current at high reverse bias with the measured low-frequency noise phenomena.

## II. DEVICE PROCESSING

The measurements and modeling presented in this study characterize front-illuminated, ion-implanted  $n^+$  on bulk  $p$ - $\text{Hg}_{1-x}\text{Cd}_x\text{Te}$  photodiodes with  $x \approx 0.22$ , operating near 77 K, used for hybrid focal plane arrays in the 8–12  $\mu\text{m}$  spectral region. The major features of the photodiodes are the following:

(i) The starting material is either (a) gold doped bulk material grown by the method of solid-state recrystallization, or (b) undoped crystals from Cominco, Inc. in which  $p$ -type conductivity is obtained with Hg vacancies.<sup>5</sup>

(ii) The junctions are planar and the junction periphery is covered by a metallic guard ring that is connected to the  $n^+$  region.

(iii)  $n^+$  shallow junctions are formed by implanting boron with a relatively low dose ( $3 \times 10^{13} \text{ cm}^{-2}$ ) and low energy ( $\approx 125 \text{ keV}$ ).

(iv) The diodes are passivated with native sulfides ( $\approx 300 \text{ \AA}$ ) and evaporated ZnS.<sup>6</sup>

(v) The junctions and photodiodes are exposed to a low-temperature postimplantation anneal ( $\approx 95^\circ \text{C}$ ) and temperature cycles up to  $85^\circ \text{C}$ .

### III. SURFACE PASSIVATION

The surfaces are characterized with metal-insulator-semiconductor (MIS) structures, gate-controlled diodes, and variable area diodes which demonstrate that surface effects do not contribute significant dark currents in properly processed photodiodes.

The electrical properties of the interfaces are defined by the measured capacitance-voltage characteristics of a MIS device<sup>7</sup> (see Fig. 1). The capacitor exhibits high-frequency behavior at 1 MHz. The surface is practically at flat band with zero gate voltage and the fixed surface state density in the interface is of the order of  $5 \times 10^{10} \text{ cm}^{-2}$ . The interface is also characterized with a low fast and slow interface trap density as indicated by the correspondence between the calculated and measured characteristics and the near absence of a hysteresis.

The major effect of the surface potential upon HgCdTe diode performance is demonstrated with gate-controlled diodes and is shown in Fig. 2. The characteristics of Fig. 2 show the diode reverse voltage as a function of gate voltage for various values of reverse voltage as a parameter, at two temperatures. For negative gate voltages that accumulate

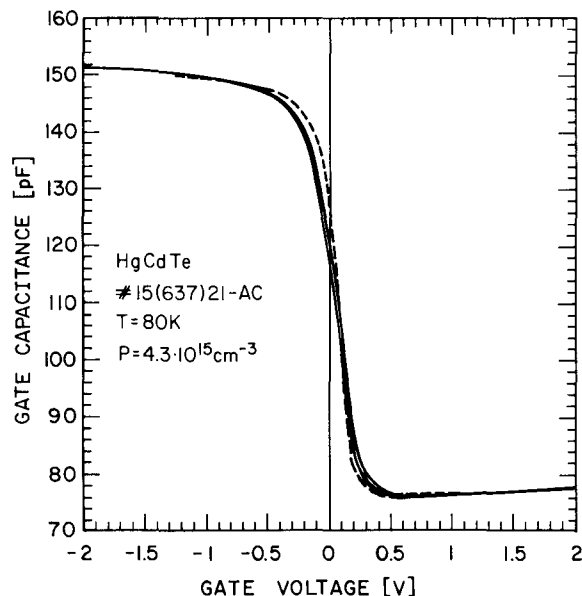
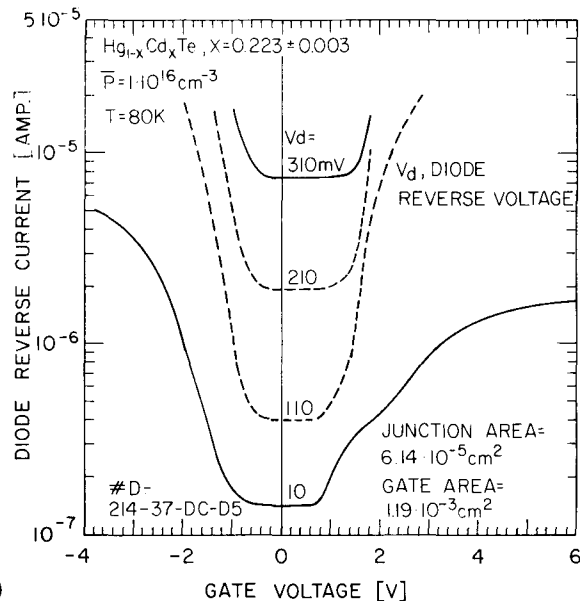
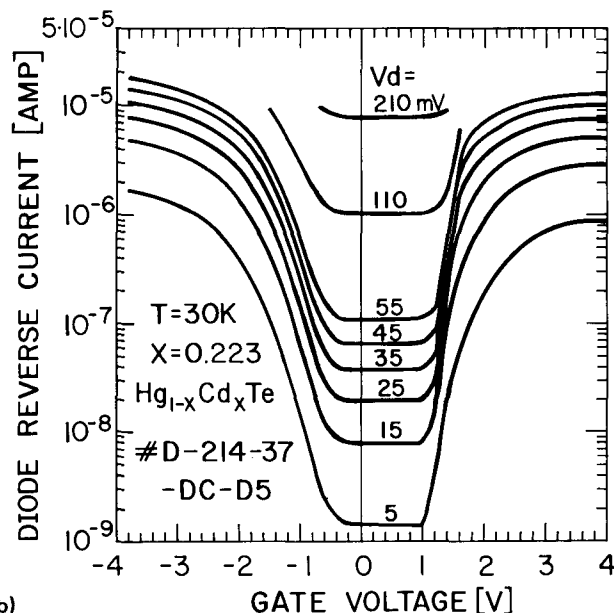


FIG. 1. Measured and calculated capacitance-voltage characteristics of a MIS capacitor. The gate is titanium ( $\approx 1000 \text{ \AA}$ ) and gold ( $\approx 1.5 \mu\text{m}$ ). The insulator is  $\sim 300\text{-\AA}$  native sulfide and  $800\text{-\AA}$  evaporated ZnS. The gate capacitor area is  $2.88 \times 10^{-3} \text{ cm}^2$ . The measurement frequency is 1 MHz and the ac oscillation level is 30 mV. The MIS device is bonded in an experimental Dewar and is not illuminated. The flat band capacitance is 126 pF.



(a)



(b)

FIG. 2. Diode reverse current as a function of gate voltage, with junction reverse voltage as a parameter: (a) at 80 K and (b) at 30 K. The junction area is  $6.144 \times 10^{-5} \text{ cm}^2$  and the gate area is  $1.19 \times 10^{-3} \text{ cm}^2$ . The composition  $x$  is 0.223. The substrate doping level is  $N_A \approx 10^{16} \text{ cm}^{-3}$ . The gate insulator (ZnS) thickness is  $3000 \text{ \AA}$ .

the surface, and for positive gate voltages that invert the surface, the diode reverse current increases exponentially (up to saturation values).

In the case of an accumulated  $p$ -type surface (negative gate voltage), the dark current is due to surface tunneling across the  $p^+-n^+$  surface junction. The  $p^+$  surface concentration is determined by the surface potential, which is controlled by the gate voltage. In the case of inverted surface (positive gate voltage) the dark current is due to tunneling currents in the field-induced junction ( $n^+p$ ) at the surface under the gate. The  $n^+$  inversion layer concentration is determined by the surface potential and hence the gate voltage, while the  $p$  concentration is determined by the substrate doping level. The field-induced junction is more abrupt than the

ion-implanted junction because additional processes, such as Hg diffusion, affect the electrical profile of ion-implanted junction (discussed in Sec. IV).

Minimum reverse currents are obtained around zero gate voltage when the surface is practically at flat band (see Fig. 1). Figure 2 shows that around zero gate voltage, the reverse current is independent of the gate voltage, regardless of the value of the reverse bias, at 80 K as well as at 30 K.

The dependence of measured diode differential resistance at zero bias voltage on temperature, for the diode of Fig. 2, is shown in Fig. 3.  $R_0$  increases with decreasing temperature up to a saturation level of  $4 \times 10^6 \Omega$ , at  $\sim 50$  K and below. The temperature dependence indicates that the diode is diffusion limited at 77 K and that the  $R_0$  is not limited by the surface passivation at that temperature.

The results of Figs. 1–3 demonstrate that with proper passivation, photodiodes which do not require a separate gate electrode to control the surface potential can be realized. In addition, we have characterized diodes with a variable junction area in a wide area ratio of 1:4:16, and we have obtained identical normalized current–voltage characteristics. In the following modeling we assume that in properly processed photodiodes, with junction area larger than  $50 \times 50 \mu\text{m}^2$ , surface effects do not contribute significant dark currents.

#### IV. CAPACITANCE–VOLTAGE (C–V) PROFILING OF HgCdTe JUNCTIONS

The complex electrical profiles observed in implanted  $\text{Hg}_{1-x}\text{Cd}_x\text{Te}$  junctions are characterized with measurements of the junction capacitance as a function of the diode reverse voltage. The measured junction capacitance–reverse voltage characteristics of ion-implanted junctions in doped and undoped  $p$ -HgCdTe substrates are shown in Fig. 4(a). With appropriate differentiation of the capacitance–voltage characteristics of large-area diodes, we evaluate the impurity distribution at the junction with fairly good accuracy. The impurity concentration  $N$  at the edge of the depletion region width  $x$  is derived by

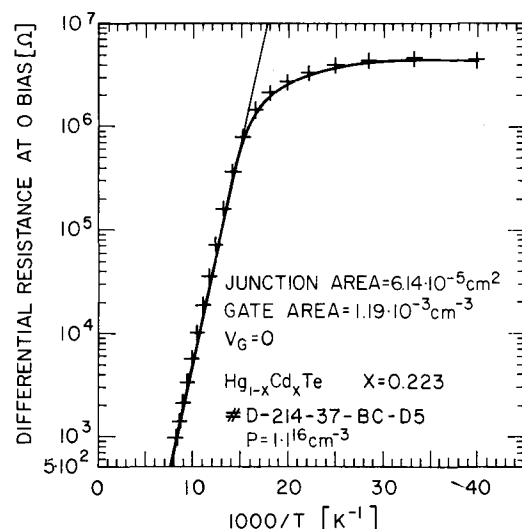


FIG. 3. The dependence of the measured diode differential resistance at zero bias (and zero gate voltage) on temperature. The diode characteristics and details are given in Fig. 2.

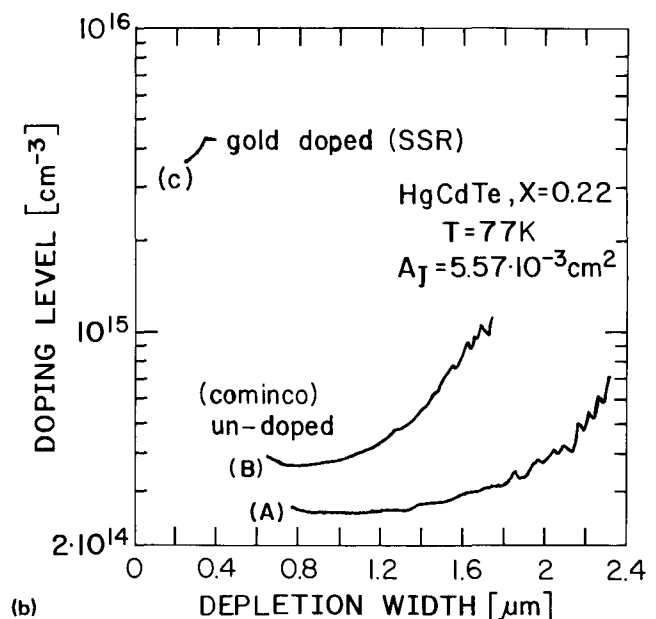
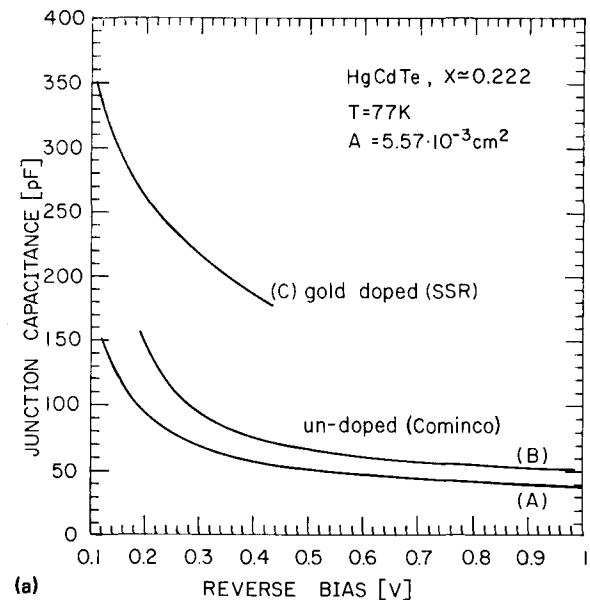


FIG. 4. (a) Measured junction capacitance as a function of diode reverse voltage, at 77 K. The junction area is  $5.57 \times 10^{-3} \text{ cm}^2$ . The measurements are performed on nonilluminated photodiodes bonded in an experimental Dewar. The measurement frequency is 1 MHz and the oscillation level is 10 mV. (b) Calculated depletion region doping level as a function of depletion region width for the diodes of (a). Curve (A): Cominco, undoped material wafer p-3383-51-AB. Composition  $x = 0.225$ . Substrate doping level is  $p = 7.45 \times 10^{15} \text{ cm}^{-3}$ . Curve (B): Cominco, undoped material, wafer 15(880)-19-AD. Composition  $x = 0.223$ . Substrate doping level is  $p = 1.1 \times 10^{16} \text{ cm}^{-3}$ . Curve (C): SSR gold doped material, wafer 716-3\*  $x = 0.222$ . Substrate doping level is  $p = 1.1 \times 10^{16} \text{ cm}^{-3}$ .

$$N(x) = \frac{2}{q\epsilon_0\epsilon_s A_J^2} \left( \frac{1}{d(l/C^2)/dV} \right), \quad (1)$$

where  $\epsilon_0\epsilon_s$  is the dielectric constant of the substrate,  $A_J$  is the junction area, and  $x = A_J \cdot (\epsilon_0\epsilon_s/C)$ . The resulting doping profiles of the implanted junctions are shown in Fig. 4(b).

From the measurements of Fig. 4 it is apparent that the origin of the  $p$ -type conductivity (Hg vacancies or substitutional doping) plays a dominant role in determining the im-

purity distribution and the electrical profile of the depletion region. In the case of the undoped material from Cominco, Inc. (type b),  $n^+p$  junctions are obtained with very low  $p$ -type doping  $\approx (2-5) \times 10^{14} \text{ cm}^{-3}$  near the  $n^+$  region. The doping gradually increases, and after  $1.5 \mu\text{m}$  is about an order of magnitude lower than the bulk doping level ( $\approx 10^{16} \text{ cm}^{-3}$  at 77 K). In the case of the gold doped material, relatively abrupt  $n^+p$  junctions are formed.

The implanted junction profile is relatively complex because ion implantation does not form directly the  $n^+p$  junction. The electrical properties of the  $n^+$  region are due to induced damage that extends beyond the boron implant profile. In addition, it has been recently suggested by Bubulac *et al.*<sup>8</sup> that Hg freed by the implant annihilates vacancies and decreases the doping level in the region adjacent to the  $n^+$  region. In the case of undoped material,  $n^+p$  gradual junctions are formed, with very low  $p$ -type doping near the  $n^+$  region. In the case of gold doped material, the doping remaining in the annihilated region is consistent with the substantial doping level, and relatively abrupt  $n^+p$  junctions are formed. The process of Hg diffusion which reduces the concentration of Hg vacancies occurs even at low temperatures ( $\approx 80^\circ\text{C}$ ) and is enhanced at higher temperatures. Thus, the model is consistent with the experimental observation that low-temperature postimplant anneal plays a dominant role in determining the junction profile which strongly affects the reverse bias current-voltage characteristics.

We suggest an additional process during junction formation that determines the electrical properties of the junction: donors in the highly compensated  $p$ -type material<sup>5</sup> are gettered by the damaged  $n^+$  region. The gettering effect is probably relevant to doped as well as undoped material.

For modeling, the depletion region is characterized with an effective doping level, with a very low  $p$  region, in the case of undoped material, and with an effective doping in the case of gold doped material, resulting in a reduced concentration of traps acting as generation-recombination centers and a higher excess lifetime.

## V. MODELING OF DARK CURRENTS AND DYNAMIC RESISTANCE IN HgCdTe PHOTODIODES

We consider the mechanisms that produce the dark currents shown in Fig. 5 for  $\text{Hg}_{1-x}\text{Cd}_x\text{Te}$  photodiodes with  $x \approx 0.22$ , in various bias regions. Figure 5(a) shows the dc characteristics of gold doped material, and Fig. 5(b) shows the characteristics of undoped material. The dark current mechanisms also determine the dynamic differential resistance as a function of diode reverse bias shown in Fig. 6, for gold doped material [Fig. 6(a)] and undoped material [Fig. 6(b)], respectively.

Three distinct mechanisms dominate the dark currents:

### A. Diffusion mechanism<sup>1,9</sup>

In the zero-bias and low-bias regions ( $\approx \pm 50 \text{ mV}$  at 77 K), diffusion current is the dominant current down to  $\sim 60 \text{ K}$ . The major contribution is from the  $p$ -side diffusion current, and hence

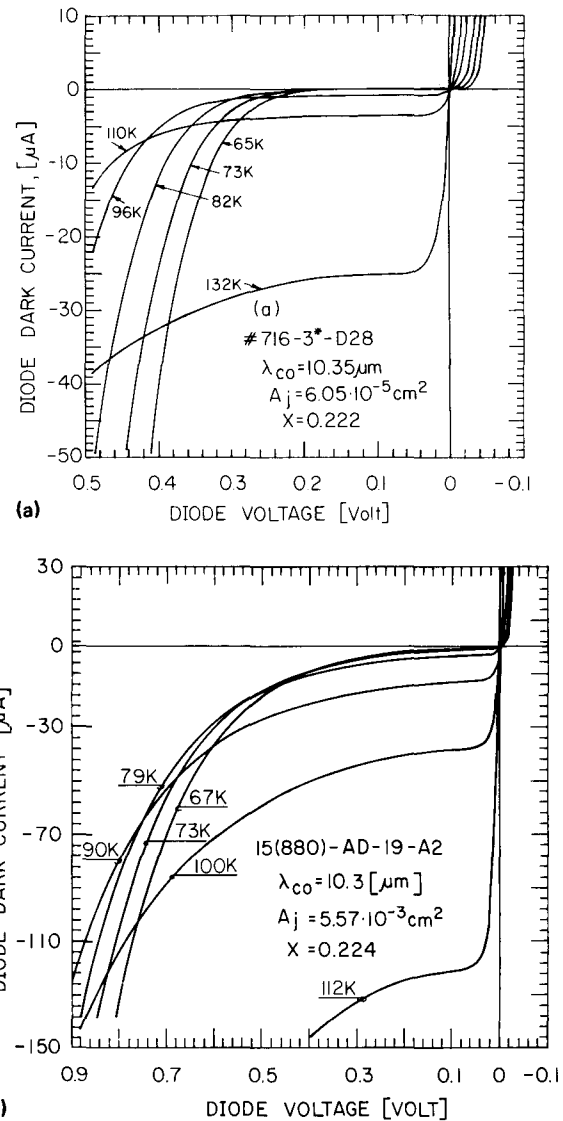


FIG. 5. Measured current-voltage characteristics of  $\text{Hg}_{1-x}\text{Cd}_x\text{Te}$  photodiodes with  $x \approx 0.22$  with diode temperature as a parameter: (a) fabricated on gold doped (SSR) material and (b) fabricated on undoped (Cominco) material.

$$I_d = qA_j \frac{n_i^2}{P_0} \left( \frac{kT}{q} \cdot \frac{\mu_n}{\tau_n} \right)^{1/2} (e^{qV/kT} - 1), \quad (2)$$

where  $P_0$  is the equilibrium doping level of the substrate,  $n_i$  is the bulk intrinsic carrier concentration, and  $A_j$  is the junction area.  $\mu_n$  and  $\tau_n$  are the minority carrier (electron) mobility and lifetime, respectively. The associated dynamic resistance defined by  $R = (dI/dV)^{-1}$  is given by

$$R_d = \frac{1}{A_j} \frac{1}{q} \frac{P_0}{n_i^2} \left( \frac{kT}{q} \frac{\tau_n}{\mu_n} \right)^{1/2} e^{-qV/kT}. \quad (3)$$

According to the diffusion mechanism, the dominant temperature dependence of the dynamic resistance at zero bias  $R_0$  is due to  $n_i^2$ , but the temperature dependence of  $\mu_n$  and  $\tau_n$  should also be included in the modeling.<sup>9</sup> By measuring the temperature dependence of  $R_0$ , the validity of the diffusion model is confirmed (see Fig. 3 and Ref. 9). Below 60 K an additional mechanism, trap-assisted tunneling, contributes significantly to  $R_0$ , and below 50 K this mechanism becomes

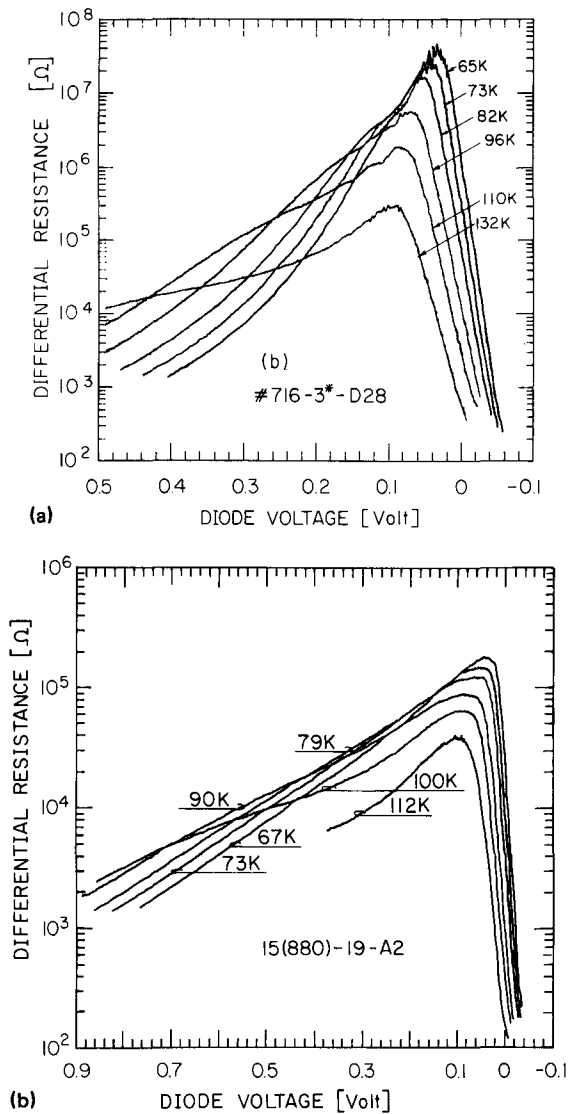


FIG. 6. Dynamic differential resistance-voltage characteristics of the photodiodes of Fig. 5 with diode temperature as a parameter: (a) Fabricated on gold doped (SSR) material and (b) undoped (Cominco) material.

the dominant one (trap-assisted tunneling is the next mechanism to be discussed.)

Around 77 K, in the low-bias region, diffusion current dominates the dark current, and the dynamic resistance is calculated with Eq. (3). The slope of the  $R_d(V)$  characteristics at this region corresponds to  $q/kT$  and decreases with increasing  $T$ . Hence, the diffusion dominated reverse-bias region expands as temperature increases. With increased forward bias,  $R_d$  decreases exponentially with the voltage, and eventually the series resistance of the device determines the measured resistance. With increased reverse bias,  $R_d$  increases exponentially, and eventually a different mechanism becomes dominant in determining the dynamic resistance of the device. The measured and calculated diffusion characteristics are compared in Figs. 7(a), 8, and 9.

The diffusion current is essentially determined by the neutral  $p$ -type substrate at a diffusion length  $L_n$ , from the edge of the depletion region. The diffusion length is at least  $10\ \mu\text{m}$ , even for a low-grade material with  $\tau_n \approx 3\ \text{ns}$ . Thus, for diffusion modeling, the relevant parameters are the substrate pa-

rameters, as determined by Hall measurements, photoconductivity measurements, admittance measurements of MIS capacitors in inversion, etc.

## B. Trap-assisted tunneling<sup>2,3,10-14</sup>

The physics and behavior of the trap-assisted tunneling mechanism have not been established yet. Dewames *et al.*<sup>2,3</sup> who carried out  $I$ - $V$  measurements over a wide temperature and bias range, showed the existence of two types of tunneling: trap assisted and band to band. Although they demonstrated the different temperature dependencies of the two mechanisms, the temperature dependence of trap-assisted tunneling remains unexplained.

Below 50 K, the measured zero-bias resistance  $R_0$  is almost independent of the temperature (see Fig. 3) and there-

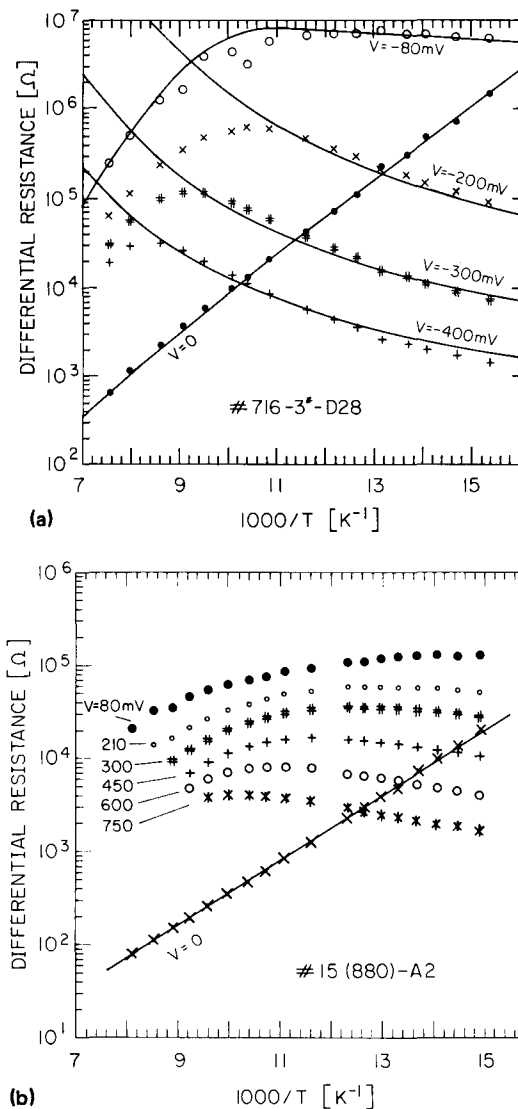


FIG. 7. Dependence of the dynamic resistance of the diodes of Fig. 5 as a function of temperature, with the diode reverse-bias voltage as a parameter. (a) For the gold doped (SSR) material measured and calculated (solid curves) data are shown. For the trap-assisted tunneling mechanism  $c$  is calculated with Eq. (8) with  $N_A$  (depletion)  $= 4 \times 10^{15}\ \text{cm}^{-3}$  [see Fig. 4(b)] and with  $B = 3 \times 10^{26}\ \text{cm}^2\ \text{s}^{-1}$ . Band-to-band tunneling is modeled with  $N_A = 1.1 \times 10^{16}\ \text{cm}^{-3}$ . (b) For the undoped (Cominco) material only measured data are presented.

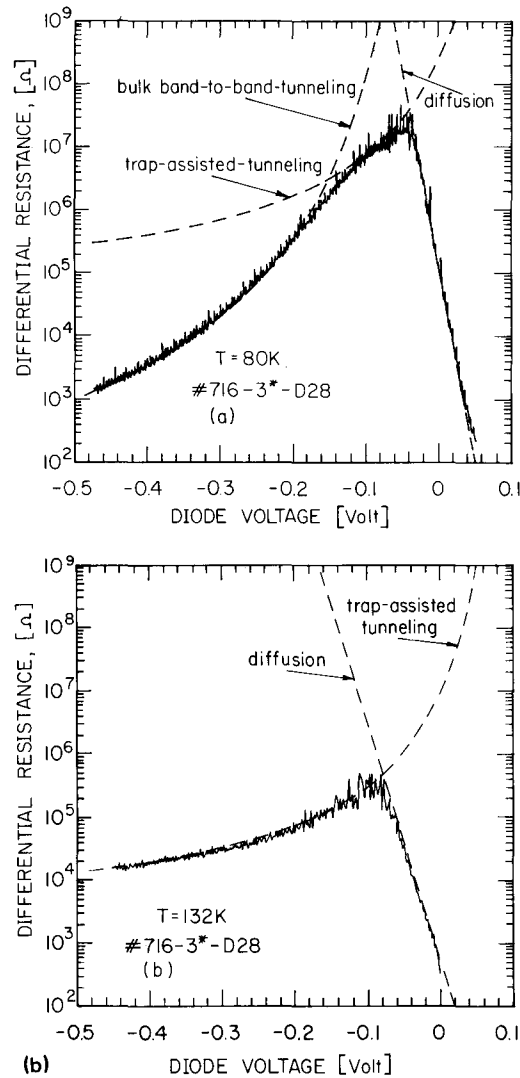


FIG. 8. The dependence of the measured (solid curve) and calculated (dashed curves) dynamic resistance upon reverse-bias voltage of the diode of Fig. 5(a). At (a)  $T = 80$  K; trap-assisted tunneling is modeled with  $c = 5.6$  V<sup>1/2</sup>,  $B = 8.25 \times 10^{19}$  cm<sup>-2</sup> s<sup>-1</sup>, and  $N_A$  (depletion) =  $4 \times 10^{15}$  cm<sup>-3</sup>. Bulk band-to-band tunneling is modeled with  $N_A = 1.1 \times 10^{16}$  cm<sup>-3</sup>. At (b)  $T = 132$  K; trap-assisted tunneling is modeled with  $c = 5.3$  V<sup>1/2</sup>,  $B = 1.21 \times 10^{21}$  cm<sup>-2</sup> s<sup>-1</sup>. Bulk band-to-band tunneling is modeled with  $N_A = 1.1 \times 10^{16}$  cm<sup>-3</sup>. The calculated total dynamic resistance, which is the sum of the three mechanisms (in parallel), coincides with the measured characteristics.

fore obviously the mechanism determining  $R_0$  at lower temperatures is not a thermal one. It is also not surface related, since the measured  $R_0$  of Fig. 3 is obtained with zero gate voltage and the data of Fig. 2 demonstrate that surface effects do not contribute dark currents at this gate voltage. Tunneling is the most plausible mechanism, but the calculated band-to-band tunneling temperature dependence corresponds to a decrease in  $R_0$  when the temperature is reduced. Therefore, bulk band-to-band tunneling is ruled out and the origin of the dark current at zero bias below 50 K is attributed to trap-assisted tunneling.

At 77 K, and for medium reverse bias, trap-assisted tunneling produces the dark current. This mechanism is examined by measuring the temperature dependence of the diode dynamic resistance shown in Fig. 7 and by the fit between the

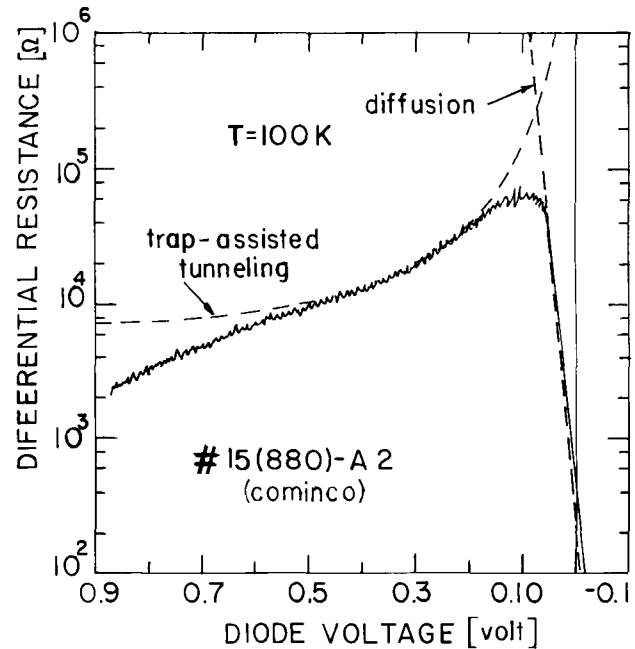


FIG. 9. The dependence of the measured (solid curve) and calculated (dashed curves) dynamic resistance upon reverse-bias voltage of the diode of Fig. 5(b), at  $T = 100$  K; Trap-assisted tunneling is modeled with  $c = 3$  V<sup>1/3</sup>,  $B = 2.1 \times 10^{18}$  cm<sup>-2</sup> s<sup>-1</sup>.

calculated and measured voltage dependencies at a given temperature, shown in Figs. 8 and 9. By following the same arguments which were applied to the zero-bias resistance  $R_0$  below 50 K, we conclude that for medium reverse bias, the dominant mechanism determining the dynamic resistance is trap-assisted tunneling. Below 100 K, the measured dynamic resistance at  $V_d = 80$  mV, for the gold doped material, does not depend upon temperature, as shown in Fig. 7(a). The undoped material exhibits the same behavior at a wider medium reverse-bias region, as shown in Fig. 7(b). Therefore, this medium is obviously not a thermal one. Calculated bulk band-to-band tunneling resistance characteristics, exhibit a pronounced temperature dependence and are therefore ruled out.

For the gold doped material, modeling the dark current with trap-assistance tunneling gives the correct temperature behavior dependence of Fig. 7 as well as the correct voltage dependence of Fig. 8. For diode reverse bias of 80 mV, and for temperatures above 100 K, diffusion becomes the dominant mechanism, as shown in Fig. 7(a). (As discussed before, the slope of  $R_d$  upon voltage is inversely proportional to  $T$ .) It is possible that in a narrow temperature range at medium reverse bias and  $\sim 100$  K, generation-recombination mechanism contributes to the measured current.

Trap-assisted tunneling is calculated with a one-dimensional, highly simplified model, assuming a simple triangular barrier for tunneling between traps and the conduction band of the  $n^+$  region. The tunneling probability  $T$ , is given with<sup>10</sup>

$$T = \exp\left(-\frac{4(2m_c^*)^{1/2}(E_g - E_t)^{3/2}}{3q\hbar E}\right), \quad (4a)$$

where  $E$  [V/cm] is the maximum electric field associated

with the barrier, and  $E_t$  is the trap energy in volts, relative to the valence band.

Following Kinch,<sup>10</sup> we assume that the effective mass of the electron is given with  $m_e^*/m_0 = 7 \times 10^{-2} E_g$ , where  $E_g$  is the band gap in volts,  $m_e^*$  is the electron mass, and  $m_0$  is the electron rest mass. Finally we obtain

$$T = \exp\left(-\frac{1.7 \times 10^7 E_g^{1/2} (E_g - E_t)^{3/2}}{E}\right). \quad (4b)$$

For a step junction, corresponding to the junction profile of gold doped material, assuming  $E = (qN_A W_t / \epsilon_0 \epsilon_s)$ , where  $W_t$  is the depletion region width, we obtain

$$T = \exp\left(-\frac{4.3 \times 10^{10} E_g^{1/2} (E_g - E_t)^{3/2}}{N_A^{1/2} V_t^{1/2}}\right) = \exp\left(\frac{-c}{V_t^{1/2}}\right), \quad (5)$$

where  $V_t = V_{bi} + V_d$  is the total junction potential and is the sum of the built-in potential  $V_{bi}$ , and the diode reverse voltage  $V_d$ . Hence, for the gold doped material, the trap-assisted tunneling current in the gold doped material  $I_t$ , is modeled for reverse bias and for  $V_d \gg V_{bi}$  with

$$I_t = qA_j B \exp\left(\frac{-c}{V_t^{1/2}}\right), \quad (6)$$

where  $B$  is constant. The calculated dynamic resistance  $R_t$  is given by

$$R_t = \frac{2}{qA_j B c} \exp\left(\frac{c}{V_t^{1/2}}\right) V_t^{3/2}. \quad (7)$$

Our assumption is that the dominant energy trap in the trap-assisted tunneling process, coincides with the Fermi level and  $E_t = E_g - E_i - E_F$ . The Fermi level is calculated with  $E_F - E_i = kT \ln[N_A (\text{depletion})/n_i]$ , where  $N_A$  is the effective doping at the depletion region obtained from the  $C$ - $V$  junction profiling of Fig. 4. The intrinsic energy level  $E_i$  is measured relative to the conduction band, while  $E_t$  is measured relative to the valence band. The constant  $c$  is calculated with

$$c = \left(\frac{4.3 \times 10^{10} E_g^{1/2} (E_g - E_t)^{3/2}}{N_A (\text{depletion})^{1/2}}\right). \quad (8)$$

The voltage dependence of the trap-assisted tunneling dynamic resistance  $R_t$  is determined by the exponential function  $\exp[c/V_t^{1/2}]$  [see Eq. (7)]. For the gold doped material, the fit between the calculated and measured dynamic resistances in the medium bias region, shown in Fig. 8, is quite good.

In the case of undoped material, the bias region in which the dynamic resistance is dominated by trap-assisted tunneling, is much wider, as shown in Figs. 7(b) and 9. Because of the more complex junction profile of undoped material, the simple modeling expressed by Eqs. (4)–(8) is unsatisfactory.

For implanted junction in HgCdTe, formed in doped as well as in undoped material, a more rigorous model for trap-assisted tunneling is required, and this mechanism should be further studied. The crude model presented, using one fitting parameter, explains the bias dependence of the trap-assisted

tunneling mechanism, as well as the temperature dependence in the low-temperature region. The model is relevant to well-behaved, high-quality photodiodes, where surface effects do not contribute significant current. Nevertheless, the temperature dependence of this mechanism above 100 K (associated with the temperature dependence of the fitting parameter) remains unexplained.

### C. Bulk band-to-band tunneling<sup>15–18</sup>

In the higher reverse bias region and at low temperatures, band-to-band tunneling current is the dominant dark current, in doped as well as in undoped material. When this mechanism dominates, the dark current increases and the diode dynamic resistance decreases, as the temperature is reduced (for a given reverse bias). The calculated bulk band-to-band tunneling current  $I_{\text{btb}}$ , and dynamic resistance  $R_{\text{btb}}$ , are compared with the measured characteristics of the gold doped material, and an excellent fit is obtained (see Figs. 7 and 8).

For modeling, we use the simple approach presented in Ref. 18. The bulk band-to-band tunneling current  $I_{\text{btb}}$  is given by

$$\frac{I_{\text{btb}}}{A_j} = \frac{q}{4\pi^2} \frac{E_g kT}{P^2} \int_{-E_{\text{max}}}^0 T(E/2) dE, \quad (9)$$

where  $P = 1.35 \times 10^{-28}$  [J m] is the matrix element,  $E_{\text{max}} = -qV_d + E_f - E_v$  and  $E_f$  and  $E_v$  are the Fermi energy and the valence-band energy, respectively. The band-to-band tunneling probability is given with

$$T = \exp\left(-\left(\frac{2m^*}{\hbar^2}\right)^{1/2} \left(\frac{2\epsilon_0 \epsilon_s}{q^2 N_A}\right)^{1/2} E_g \left\{\left(1 - \frac{E}{E_g}\right) \times \left[\frac{\pi}{2} - \sin^{-1}\left(\frac{-E}{E_g - E}\right)^{1/2}\right] - \left(\frac{-E}{E_g}\right)^{1/2}\right\}\right). \quad (10)$$

With proper differentiation, the bulk band-to-band tunneling dynamic resistance  $R_{\text{btb}}$  is obtained:

$$R_{\text{btb}}^{-1} = \left(\frac{q^2}{A_j \cdot 4\pi^2} \frac{E_g kT}{P^2}\right) T(E_{\text{max}}/2). \quad (11)$$

Similar results are obtained with the more rigorous theory developed by Anderson<sup>15</sup> and studied in detail in Ref. 17. However, in this approach, to obtain a proper fit between the calculations and the measurements, an effective low doping level should be introduced in the modeling. This is consistent with the junction profiling of Sec. IV.

It is evident that with the relatively abrupt junction obtained in the gold doped material, bulk band-to-band tunneling is observed at lower reverse voltages. In the case of undoped material, with gradual  $n^+p^-p$  junctions characterized by the very low  $p$ -type doping near the  $n^+$  region, the bulk band-to-band tunneling is shifted to higher reverse voltages. Bulk band-to-band tunneling is not significant up to  $\sim 1$  V [see Fig. 7(b)].

## VI. SPECTRAL NOISE CURRENT

The correlation between  $1/f$  noise phenomena and tunneling processes in HgCdTe photodiodes was previously suggested.<sup>2,12</sup> Empirical correlation between the  $1/f$  noise



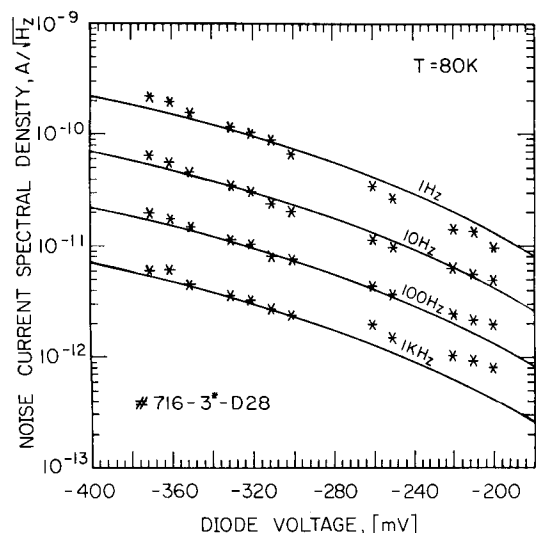


FIG. 10. Measured and calculated (solid curves) noise current spectral density of the photodiode with the dc characteristics of Fig. 5(a) at 80 K, in the frequency range 1 Hz–1 kHz. The reference shot noise level  $(2qI)^{1/2}$  for  $I = 200$  nA measured at reverse bias 200 mV, is  $1.78 \times 10^{-13}$  [A/Hz $^{-1/2}$ ].

and the tunneling dark current of gate-controlled diodes was also demonstrated.<sup>6</sup>

Figure 10 exhibits the correspondence between measured and calculated noise current spectral density of a photodiode fabricated on gold doped material [the photodiode of Fig. 5(a)], in the frequency range 1 Hz–1 kHz. In the investigated bias region of Fig. 10, bulk band-to-band tunneling dominates the dynamic resistance. In the measured frequency range, at 80 K, the modeling of the noise current is obtained with

$$i_n = \alpha \left( \frac{I_{\text{btb}}}{f} \right)^{1/2} [\text{A Hz}^{-1/2}], \quad (12)$$

where  $I_{\text{btb}}$  is calculated with Eq. (9) and  $\alpha = 10^{-7}$  [A $^{1/2}$ ].

To correlate the mechanisms that produce the dc dark current with the measured low-frequency noise phenomena, the measurements and modeling illustrated in Fig. 10 should

be studied in a wide temperature range as well as in a wide reverse-bias region.

## ACKNOWLEDGMENTS

The technical assistance of A. Zohar, N. Steinbrecher, D. Schoenmann, R. Prager, and A. Shai is acknowledged with thanks. This research was performed in the laboratories donated by Etia and Miguel Meilichson.

<sup>1</sup>M. B. Reine, A. K. Sood, and T. J. Tredwell, in *Semiconductors and Semimetals*, edited by R. K. Willardson and A. C. Beer (Academic, New York, 1981), Vol. 18, Chap. 6.

<sup>2</sup>R. E. DeWames, J. G. Pasko, E. S. Yao, A. H. B. Vanderwyck, and G. M. Williams, *J. Vac. Sci. Technol. A* **6**, 2655 (1988).

<sup>3</sup>R. E. DeWames, G. M. Williams, J. G. Pasko, and A. H. B. Vanderwyck, *J. Cryst. Growth* **86**, 849 (1988).

<sup>4</sup>R. Balcerak, J. F. Gibson, W. H. Gutierrez, and J. H. Pollar, *Opt. Eng.* **26**, 191 (1987).

<sup>5</sup>E. Finkman and Y. Nemirovsky, *J. Appl. Phys.* **59**, 1205 (1986).

<sup>6</sup>Y. Nemirovsky, R. Adar, A. Kornfeld, and I. Kidron, *J. Vac. Sci. Technol. A* **4**, 1986 (1986).

<sup>7</sup>Y. Nemirovsky and I. Bloom, *J. Vac. Sci. Technol. A* **6**, 2710 (1988).

<sup>8</sup>L. O. Bubulac and W. E. Tennant, *Appl. Phys. Lett.* **51**, 355 (1987).

<sup>9</sup>Y. Nemirovsky and D. Rosenfeld, *J. Appl. Phys.* **63**, 2435 (1988).

<sup>10</sup>M. A. Kinch, in Ref. 1, Chap. 7.

<sup>11</sup>W. W. Anderson and H. J. Hoffman, *J. Appl. Phys.* **53**, 9130 (1982).

<sup>12</sup>W. W. Anderson and H. J. Hoffman, *J. Vac. Sci. Technol. A* **1**, 1730 (1983).

<sup>13</sup>D. K. Blanks, J. D. Beck, M. A. Kinch, and L. Colombo, *J. Vac. Sci. Technol. A* **6**, 2790 (1988).

<sup>14</sup>J. D. Beck, M. A. Kinch, E. J. Espotco, and R. A. Chapman, *J. Vac. Sci. Technol.* **21**, 172 (1982).

<sup>15</sup>W. W. Anderson, *Infrared Phys.* **20**, 353 (1987).

<sup>16</sup>W. A. Beck and N. E. Byer, *IEEE Trans. Electron Devices* **31**, 292 (1984).

<sup>17</sup>R. Adar, Y. Nemirovsky, and I. Kidron, *Solid State Electron.* **30**, 1289 (1987).

<sup>18</sup>Y. Nemirovsky and I. Bloom, *Infrared Phys.* **27**, 143 (1987).